Wing kinematics measurement and aerodynamics of hovering droneflies

Yanpeng Liu* and Mao Sun

Institute of Fluid Mechanics, Beijing University of Aeronautics and Astronautics, Beijing 100083, People's Republic of China

*Author for correspondence (e-mail: liuyanpeng1980@163.com)

SUMMARY

The time courses of wing and body kinematics of three freely hovering droneflies (*Eristalis tenax*) were measured using 3D high-speed video, and the morphological parameters of the wings and body of the insects were also measured. The measured wing kinematics was used in a Navier–Stokes solver to compute the aerodynamic forces and moments acting on the insects. The time courses of the geometrical angle of attack and the deviation angle of the wing are considerably different from that of fruit flies recently measured using the same approach. The angle of attack is approximately constant in the mid portions of a half-stroke (a downstroke or upstroke) and varies rapidly during the stroke reversal. The deviation angle is relatively small and is higher at the beginning and the end of a half-stroke and lower at the middle of the half-stroke, giving a shallow U-shaped wing-tip trajectory. For all three insects considered, the computed vertical force is approximately equal to the insect weight (the difference is less than 6% of the weight) and the computed horizontal force and pitching moment about the center of mass of the insect are approximately zero. The computed results satisfying the equilibrium flight conditions, especially the moment balance condition, validate the computation model. The lift principle is mainly used to produce the weight-supporting vertical force, unlike the fruit flies who use both lift and drag principles to generate the vertical force; the vertical force is mainly due to the delayed stall mechanism. The magnitude of the inertia power is larger than that of the aerodynamic power, and the largest possible effect of elastic storage amounts to a reduction of flight power by around 40%, much larger than in the case of the fruit fly.

Supplementary material available online at http://jeb.biologists.org/cgi/content/full/211/13/2014/DC1

Key words: dronefly, hovering, wing kinematics measurement, aerodynamics, Navier–Stokes simulation.

INTRODUCTION

To understand the aerodynamics, energetics and control of insect flight, it is necessary to know the time history of the aerodynamic forces and moments produced by the flapping wings. It is difficult, even impossible, to directly measure the forces and moments on the wings of a freely flying insect. Existing means of circumventing this limitation are to measure experimentally or to compute numerically the forces and moments on model insect wings (e.g. Dickinson et al., 1999; Usherwood and Ellington, 2002a; Usherwood and Ellington, 2002b; Sun and Tang, 2002a).

In order to use the experimental and computational methods to obtain the aerodynamic forces and moments and to study insect flight, measurements of wing kinematics and some morphological parameters are required. Other researchers have measured wing kinematics of many insects in free flight, using high-speed cine or video; and also measured morphological data of these insects (Ellington, 1984a; Ellington, 1984b; Dudley and Ellington, 1990; Willmott and Ellington, 1997). But since these reported studies used only one camera, the continuous time variation of wing orientation (geometrical angle of attack, wing rotation rate, etc.) could not be obtained. Recently, the time course of three-dimensional (3D) wing motion of freely flying fruit flies was measured using three orthogonally aligned, high-speed cameras (Fry et al., 2005). Measurements of 3D wing motion of other insects are of great interest, but some limitations to Fry et al.'s work meant that morphological parameters such as weight and position of center of mass could not be measured. If these data were also measured, one could use them to test the experimental and computational models (a reasonable test of the experimental and computational models is

that the measured or computed vertical force approximately balances the insect weight and, in hovering flight, the horizontal force and the pitching moment about the centre of mass of the insect are approximately zero).

In the present study, we measure the time course of 3D wing motion of hovering droneflies using three orthogonally alined high-speed cameras and also measure the required morphological data, and then employ the method of computational fluid dynamics (CFD) to compute the aerodynamic forces and moments of the wings flapping with the measured kinematics. The reasons we chose droneflies are (1) droneflies might have different wing kinematics from that of fruit flies used in Fry et al.'s study, (2) they are capable of motionless hovering, and (3) they fly even in strongly lit laboratory conditions. Comparison between computed results and the conditions of vertical force being equal to weight, horizontal force being equal to zero, and moment about the center of mass being equal to zero, can provide a test of the computational model. Analyzing the time courses of the wing motion and aerodynamic forces and moments could provide insights into how the aerodynamic forces and moments are produced and how the flight balance is achieved. Using the computed results, the power requirements can be readily estimated and the aerodynamic efficiency of flight examined.

MATERIALS AND METHODS
Animals

We netted droneflies of the species *Eristalis tenax* Linnaeus in a suburb of Beijing in September 2006. All experiments were
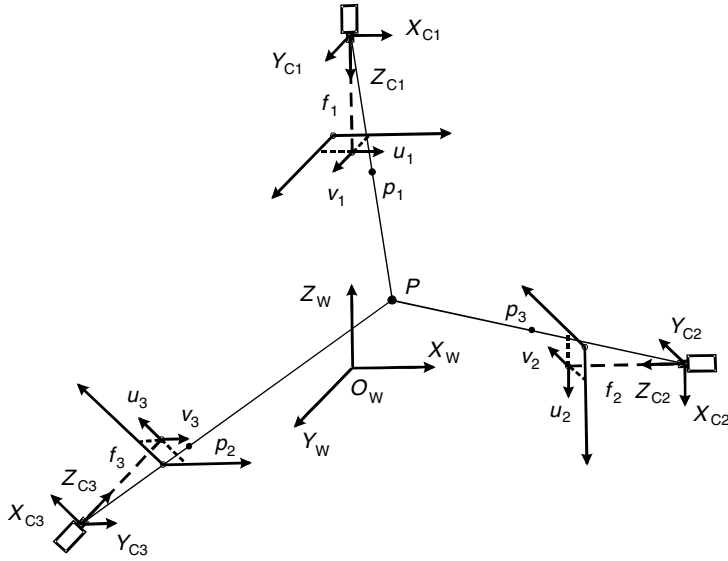
Fig. 1. Model of trinocular stereo vision system. $(X_W\ Y_W\ Z_W)$, the world coordinate system; $(X_{C1}\ Y_{C1}\ Z_{C1})$, $(X_{C2}\ Y_{C2}\ Z_{C2})$ and $(X_{C3}\ Y_{C3}\ Z_{C3})$, the camera coordinate systems of cameras 1, 2 and 3, respectively; $(u_1\ v_1)$, $(u_2\ v_2)$ and $(u_3\ v_3)$, image coordinate systems of camera 1, 2 and 3, respectively. P, an arbitrary point; p_1, p_2 and p_3, the projective points and f_1, f_2 and f_3, the focal length of cameras 1, 2 and 3, respectively.

conducted in the same day of capture. Only the most vigorous individuals were selected for filming.

3D high-speed film

We filmed the hovering flight of the droneflies in an enclosed flight chamber using three orthogonally aligned synchronized high-speed cameras (MotionXtra HG-LE, 5000 frames s⁻¹, shutter speed 50 μs, resolution 512×320 pixels). The flight chamber, a cube of $15\times15\times15$ cm³, was built from translucent glass. We backlit each camera view using densely packed arrays of light emitting diodes (LED) covered with diffusion paper. The reason we used LED arrays as the light source was that they produced much less heat than cine lights at the elevated light levels required for high-speed filming. The filming was started only when the insect hovered in the cubic zone of approximately $5\times5\times5$ cm³ at the central region of the chamber, which represented the intersecting field of views of the the three cameras.

Measurement of wing and body kinematics

Using a flat calibration panel to calibrate the cameras, one can obtain the transform matrices between the world coordinate system and three image coordinate systems, which are called projection matrices. Based on the basic principles of stereo vision, the projections of the scene point in the world coordinate system onto any image coordinate system can be calculated, provided that the point's coordinate in the world coordinate system and projection matrices are known. The general structure of a trinocular stereo vision system is shown in Fig. 1.

Let $(X_w\ Y_w\ Z_w)$ be the world coordinate system; let $(X_{C1}\ Y_{C1}\ Z_{C1})$, $(X_{C2}\ Y_{C2}\ Z_{C2})$ and $(X_{C3}\ Y_{C3}\ Z_{C3})$ be the camera coordinate systems of camera 1, 2 and 3, respectively; let $(u_1\ v_1)$, $(u_2\ v_2)$ and $(u_3\ v_3)$ be the image coordinate systems of cameras 1, 2 and 3, respectively. Let P be an arbitrary point, whose coordinates are X_w, Y_w and Z_w in the world frame, X_{C1}, Y_{C1} and Z_{C1} in the frame of camera 1, X_{C2}, Y_{C2} and Z_{C2} in the frame of camera 2, X_{C3}, Y_{C3} and Z_{C3} in the frame of camera 3. Let p_1, p_2 and p_3 be the projective points of P on the three cameras; p_1's coordinates in the image frame of camera 1 are u_1 and v_1; p_2's coordinates in the image frame of camera 2 are u_2 and v_2; p_3's coordinates in the image frame of camera 3 are u_3 and v_3. The coordinate transformation between the world coordinate system and the three image coordinate systems are:

$$Z_{c1}\begin{bmatrix} u_1 \\ v_1 \\ 1 \end{bmatrix} = \mathbf{M}_1 \begin{bmatrix} X_w \\ Y_w \\ Z_w \\ 1 \end{bmatrix}, \quad Z_{c2}\begin{bmatrix} u_2 \\ v_2 \\ 1 \end{bmatrix} = \mathbf{M}_2 \begin{bmatrix} X_w \\ Y_w \\ Z_w \\ 1 \end{bmatrix},$$

$$Z_{c3}\begin{bmatrix} u_3 \\ v_3 \\ 1 \end{bmatrix} = \mathbf{M}_3 \begin{bmatrix} X_w \\ Y_w \\ Z_w \\ 1 \end{bmatrix}, \quad (1)$$

where $\mathbf{M}_1$, $\mathbf{M}_2$ and $\mathbf{M}_3$ are projection matrices of camera 1, camera 2 and camera 3, respectively. Let $m1_{i,j}$, $m2_{i,j}$ and $m3_{i,j}$ (i, j=1,2,3) denote the elements of $\mathbf{M}_1$, $\mathbf{M}_2$ and $\mathbf{M}_3$, respectively. Eliminating Z_{C1}, Z_{C2} and Z_{C3} from Eqn 1 gives:

$$\begin{cases} m1_{11}X_w + m1_{12}Y_w + m1_{13}Z_w + m1_{14} \\ \quad - u_1X_w m1_{31} - u_1Y_w m1_{32} - u_1Z_w m1_{33} = u_1 \\ m1_{21}X_w + m1_{22}Y_w + m1_{23}Z_w + m1_{24} \\ \quad - v_1X_w m1_{31} - v_1Y_w m1_{32} - v_1Z_w m1_{33} = v_1, \end{cases} \quad (2)$$

$$\begin{cases} m2_{11}X_w + m2_{12}Y_w + m2_{13}Z_w + m2_{14} \\ \quad - u_2X_w m2_{31} - u_2Y_w m2_{32} - u_2Z_w m2_{33} = u_2 \\ m2_{21}X_w + m2_{22}Y_w + m2_{23}Z_w + m2_{24} \\ \quad - v_2X_w m2_{31} - v_2Y_w m2_{32} - v_2Z_w m2_{33} = v_2, \end{cases} \quad (3)$$

$$\begin{cases} m3_{11}X_w + m3_{12}Y_w + m3_{13}Z_w + m3_{14} \\ \quad - u_3X_w m3_{31} - u_3Y_w m3_{32} - u_3Z_w m3_{33} = u_3 \\ m3_{21}X_w + m3_{22}Y_w + m3_{23}Z_w + m3_{24} \\ \quad - v_3X_w m3_{31} - v_3Y_w m3_{32} - v_3Z_w m3_{33} = v_3. \end{cases} \quad (4)$$
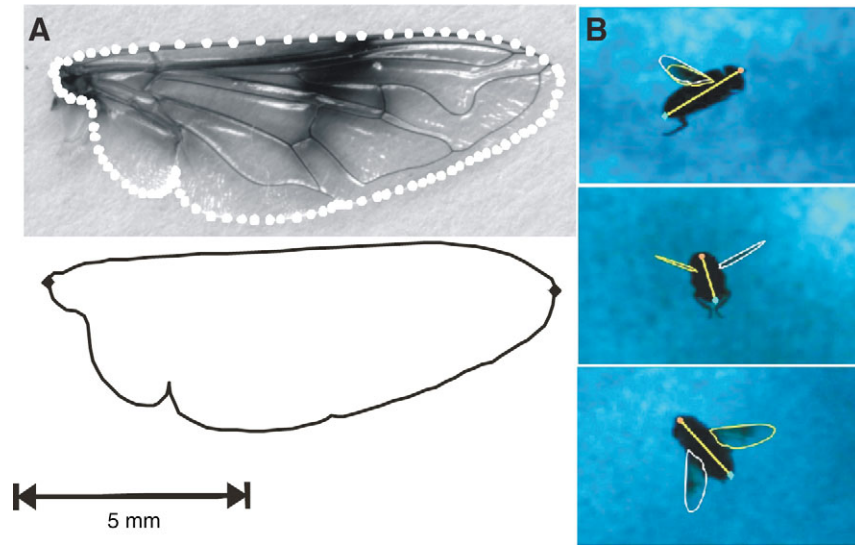
Fig. 2. (A) Wing model. (B) Example of frames recorded by the three cameras. See text for details.

The coordinates of point P's projection onto all three image coordinate systems can be determined *via* Eqn 2–4.

We take a line segment, whose length is equal to the body length of the insect, to represent the body of the insect, and used the outline of the wing obtained from scanned picture of the wing (see Fig. 2A) to represent the wing. The line segment of the body and the outline of a wing are designated as the models of the body and the wing, respectively. They can be represented as a set of points. Using the method described above, we can easily computed the projection of the point set on all the three image coordinate systems.

We developed a toolbox for Matlab (The MathWorks, Inc., Natick, MA, USA) to extract the position and attitude of the body and of the wings from images captured by all three cameras. We put the models of the body and the wings into the world coordinate system, then changed the positions and attitudes of those models until the best overlap between a model's projection and displayed frame was achieved in all three views. At this point, the positions and attitudes of those models would be taken as the positions and attitudes of the body and wings of the insect. Generally, several readjustments of each model's position and attitude were required to obtain a satisfactory overlap.

Measurement of morphological parameters

The present method of measuring the morphological parameters follows, for the most part, the detailed description of the method given by Ellington (Ellington, 1984a).

The insect was killed with ethyl acetate vapor after filming. The total mass m was measured to an accuracy of ±0.01 mg. The wings were then cut from the body and the mass of the wingless body measured. The wing mass m_{wg} was determined from the difference between the total mass and the mass of wingless body.

Immediately after cutting the wings from the body, the shape of one of them was scanned using a scanner (HP scanjet 4370; resolution 3600×3600 d.p.i.). A sample of the scanned picture of a wing is shown in Fig. 2A. Using the scanned picture, wing length R (the distance between the wing base and the wing tip) (see Ellington, 1984a) and local wing chord length were measured to an accuracy better than ±0.5%. Parameters including wing area, mean
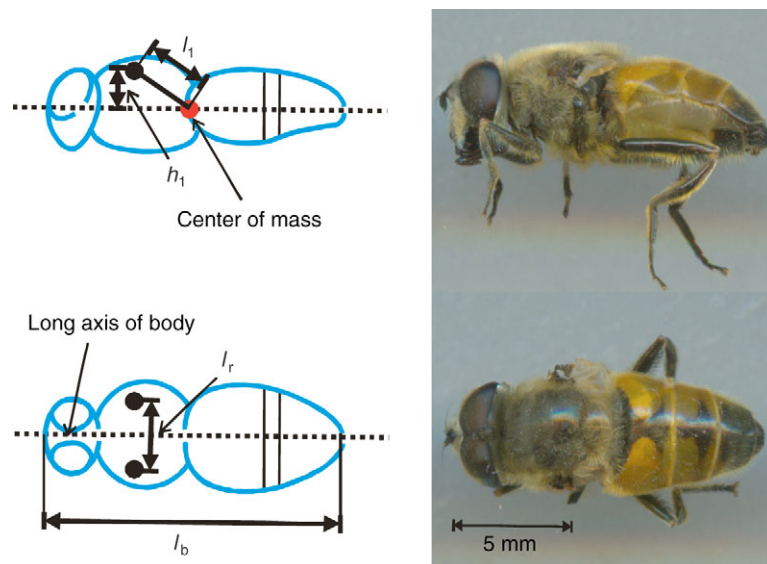

Fig. 3. Definitions of morphological parameters of wing and body. h_1, distance from wing-root axis to long-axis of body; l_1, distance from wing-root axis to body center of mass; l_r, distance between two wing roots; l_b, body length.

chord length, radius of second moment of wing area, etc., were computed using the measured wing shape.

The wingless body (with legs removed) was scanned from two perpendicular directions (the dorsoventral and lateral views; Fig. 3). Following Ellington (Ellington, 1984a), the cross section of the body was taken as ellipse and a uniform density was assumed for the body. With these assumptions and the measured body shape, the center of mass of body could be determined. Body length (l_b) and distance between the wing roots (l_r) were measured from the dorsal views; distance between the wing-base axis and the center of mass (l_1) and distance between the wing-base axis and the long axis of the body (h_1) were measured from the lateral view (the pitch moment of inertia about the center of mass could also be determined).

Computation of aerodynamic forces and moments and power requirements

The aerodynamic forces and moments were computed using the CFD method. On the basis of studies on wing–wing interactions (Lehmann et al., 2005; Sun and Yu, 2006), aerodynamic interactions between the left and right wings could be neglected. During hovering flight, the body did not move, and it was assumed that the aerodynamic interaction between the body and the wings was negligible. Therefore in the present CFD model, the body was neglected and only the flows around one wing were computed (the aerodynamic force and moment produced by the other wing were derived from the results of the computed wing). The wing planform of the insect was obtained from the present measured data. The wing section was assumed to be a flat plate with rounded leading and trailing edges, the thickness of which was 3% of the mean chord length of the wing.

The flow equations and the solution method used were the same as those described in Sun and Tang (Sun and Tang, 2002a). The computational grid had dimensions $100 \times 99 \times 105$ in the normal direction, around the wing section and in the spanwise direction, respectively (portions of the grid used for one of the insects in the present study are shown in Fig. 4). The normal grid spacing at the wall was $0.0015c$ (where c is the mean chord length of wing). The outer boundary was set at 20 chord lengths from the wing. The non-dimensional time step was 0.02 (non-dimensionalized by c/U, where U is the mean speed of wing at the radius of second moment of wing area; there are about 400 time steps in a stroke cycle). A detailed study of the numerical variables such as grid size, domain size, time step, etc., was conducted and it was shown that the above values for the numerical variables were appropriate for the calculations.

RESULTS

Three droneflies hovering at the central region of the flight chamber (the zone of the interesting field of view of the three cameras) were filmed. They were denoted as DF1, DF2 and DF3, respectively. For each of the droneflies, film of around 12 wing strokes were
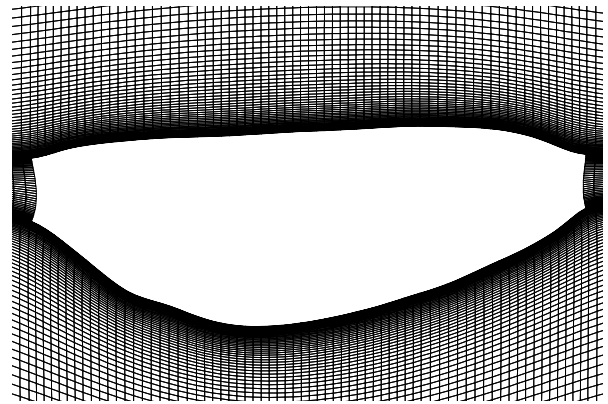

Fig. 4. A portion of the computation grid of the dronefly wing.

digitized. Samples of the original video sequences for DF1 are presented as Movie 1 in supplementary material.

Morphological parameters

Morphological parameters of insects filmed in free hovering are given in Table 1. Parameters in the table include the total mass of an insect (m), the mass of a wing (m_{wg}), the wing length (R), mean chord length of wing (c), area of a wing (S), radius of second moment of wing area (r_2), body length (l_b) and distance between the two wing roots (l_r), distance between the wing-base axis and the center of mass (l_1), distance between the wing-base axis and the long axis of the body (h_1), and the pitch moment of inertia about the center of mass (I_y).

Wing kinematics

We determine the stroke plane in the same way as that of Ellington (Ellington, 1984b). The stroke angle (ϕ), the stroke deviation angle (θ) and the angle of attack (α) of a wing are defined as in Fig. 5. The measured data of these angles as functions of time for the left and the right wings of DF1 are shown in Fig. 6 (for the three insects in hovering, about seven well-repeated wing strokes in which the left and right wings moving symmetrically are captured). As seen in Fig. 6, the motion of the right wing is approximately the same as that of the left wing, as expected for hovering flight. The stroke positional angle varies with time approximately as a sinusoidal function. The angle of attack does not vary significantly in the mid-position of the down- or upstroke, but varies sharply during the stroke reversal. The stroke deviation angle is relatively small; it is higher at the begining and the end of a downstroke or upstroke, and lower at the middle of the down- or upstroke.

Data of seven cycles for DF1 are superposed and plotted in Fig. 7. Curves of simple functions that approximately fit the data are also plotted in the figure. For a clear description of the data, we express time during a cycle as a non-dimensional parameter, $\hat{t}$, such that

Table 1. Morphological parameters of the droneflies

ID	m (mg)	m_{wg} (mg)	R (mm)	c (mm)	S (mm^2)	l_b (mm)	h_1/l_b	l_1/l_b	l_r/l_b	r_2/R	I_y (kg m^2)
DF1	88.88	0.56	11.20	2.98	33.34	14.11	0.08	0.13	0.33	0.55	1.183^{-9}
DF2	165.88	0.65	11.18	2.94	32.88	14.65	0.09	0.16	0.32	0.56	2.963^{-9}
DF3	142.69	0.63	10.65	2.90	30.83	14.16	0.09	0.14	0.31	0.55	1.893^{-9}

m, mass of the insect; m_{wg}, mass of one wing; R, wing length; c, mean chord length; S, area of one wing; l_b, body length; h_1, distance from wing-root axis to long-axis of body; l_1, distance from wing-root axis to body center of mass; l_r, distance between two wing-roots; r_2, radius of second moment of wing area; I_y, moment of inertia of the body about center of mass.
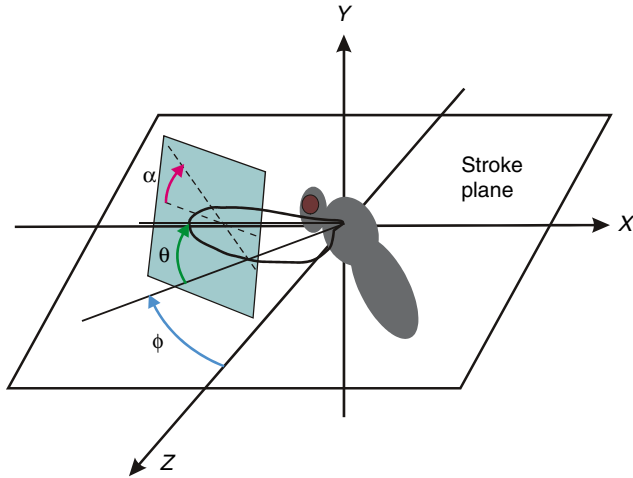
Fig. 5. Definitions of the angles of a flapping wing that determine the wing orientation. (*X Y Z*), coordinates in a system with its origin at the wing root and with *Z*-axis points to the side of the insect and *X–Z* plane coincides with the stroke plane. ϕ, the positional angle; α, geometrical angle of attack; θ, deviation angle.

$\hat{t}=0$ at the start of a downstroke and $\hat{t}=1$ at the end of the subsequent upstroke. Data of the positional angle (Fig. 7A) can be well approximated by a simple harmonic function:

$$\phi = \overline{\phi} + 0.5\Phi\sin(2\pi n t), \quad (5)$$

where *n* is the wingbeat frequency, $\overline{\phi}$ the mean stroke angle and Φ the stroke amplitude [$\overline{\phi}$ and Φ are defined as following: $\overline{\phi}=(\phi_{max}+\phi_{min})/2$, $\Phi=\phi_{max}-\phi_{min}$, where ϕ_{max} and ϕ_{min} are the maximum and minimum values of ϕ, respectively (see Ellington, 1984b)].

The time variation of the angle of attack (Fig. 7B) can be approximated by the following functions. It is a constant at the mid-position of the down- or upstroke and varies with time at the stroke reversal; the rate of its variation can be fitted by a cosine function.
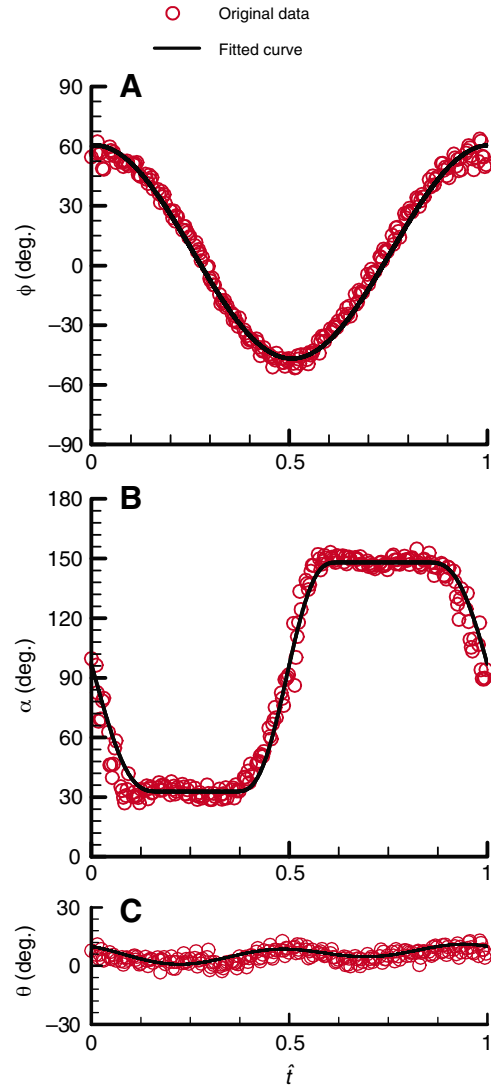

Fig. 7. Wing kinematics of DF1. ϕ, positional angle; α, geometrical angle of attack; θ, deviation angle; $\hat{t}$, non-dimensional time.

The constant of α at the mid-position of the downstroke is denoted as α_d, that of the upstroke as $180°-\alpha_u$ (α_d and α_u are the geometrical angles of attack of the downstroke and upstroke, respectively). The rotation time (non-dimensionalized by stroke period) is denoted as $\Delta\hat{t}_s$ for supination (α change from α_d to $180°-\alpha_u$) and $\Delta\hat{t}_p$ for pronation (α change from $180°-\alpha_u$ to α_d). Wing rotation may not be exactly symmetrical (wing rotation is symmetrical when the rotation occurring is symmetrical with respect to stroke reversal, i.e. half the rotation is conducted in the later part of a half-stroke and the other half in the early part of the following half-stroke); we use $\Delta\hat{t}_{s,t}$ to denote the time (non-dimensionalized by stroke period) the supination is advanced (a negative value means the rotation is delayed), and $\Delta\hat{t}_{p,t}$ to denote the non-dimensional time the pronation is advanced. The function representing the time variation of α during supination is:

$$\alpha = \alpha_d + a\left\{\left(\hat{t}-\hat{t}_1\right) - \frac{\Delta\hat{t}_s}{2\pi}\sin\left[2\pi\left(\hat{t}-\hat{t}_1\right)/\Delta\hat{t}_s\right]\right\}, \quad (6a)$$
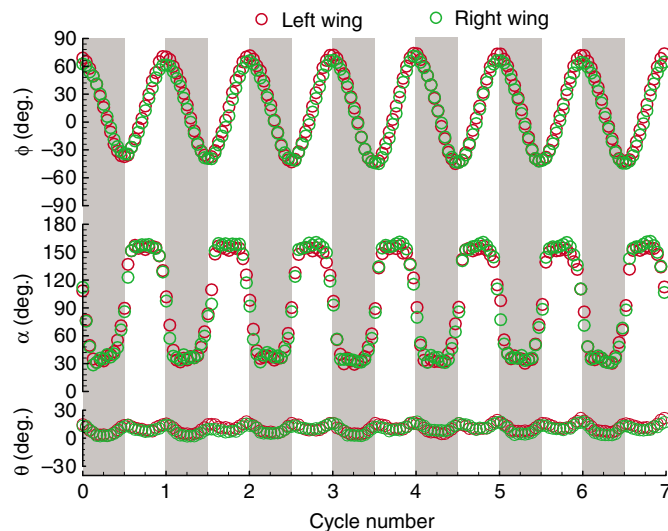

Fig. 6. Instantaneous wing kinematics of DF1 in hovering. ϕ, the positional angle; α, geometrical angle of attack; θ, deviation angle.

Table 2. Kinematic parameters of hovering droneflies

ID	n (Hz)	Φ (deg.)	$\bar{\phi}$ (deg.)	α_d (deg.)	α_u (deg.)	$\Delta\hat{t}_p$	$\Delta\hat{t}_s$	$\Delta\hat{t}_{p,t}$	$\Delta\hat{t}_{s,t}$	θ_0 (deg.)	θ_1 (deg.)	θ_2 (deg.)	η_1	η_2	β (deg.)	χ (deg.)	J
DF1	164	107.1	7.12	33.8	33.0	0.26	0.32	−0.01	−0.01	7.07	2.31	3.44	2.83	2.08	4.0	38.0	0.01
DF2	209	109.5	13.4	35.5	24.2	0.29	0.31	−0.01	0.0	10.73	2.75	3.96	2.77	1.56	16.4	29.7	0.00
DF3	142	109.1	11.9	34.2	34.2	0.30	0.31	0.03	−0.02	6.82	1.55	3.44	0.71	0.83	6.2	39.8	0.02

n, stroke frequency; Φ, stroke amplitude; $\bar{\phi}$, mean stroke angle; α_d, constant value of α at the mid-position of the downstroke; α_u, constant value of α at the mid-position of the upstroke; $\Delta\hat{t}_p$, non-dimensional time duration for pronation; $\Delta\hat{t}_s$, non-dimensional time duration for supination; $\Delta\hat{t}_{p,t}$, non-dimensional advance time for pronation; $\Delta\hat{t}_{s,t}$, non-dimensional advance time for supination; θ_0, constant value of Fourier series of deviation angle; θ_1, amplitude of the first harmonic of Fourier series of deviation angle; θ_2, amplitude of the second harmonic term of deviation angle; η_1, phase angle of the first harmonic of Fourier series of deviation angle; η_2, phase angle of the second harmonic of Fourier series of deviation angle; β, stroke plane angle; χ, body angle; J, advanced ratio.

where a is a constant:

$$a = (180° - \alpha_u - \alpha_d) / \Delta\hat{t}_s. \qquad (6b)$$

t_1 is the time when the wing-rotation starts:

$$\hat{t}_1 = 0.5 - \Delta\hat{t}_s / 2 - \Delta\hat{t}_{s,t}. \qquad (6c)$$

The expression of the pronation can be written in the same way.

Finally, the time variation of the deviation angle (Fig. 7C) can be approximately represented by the first two terms of a Fourier series:

$$\theta = \theta_0 + \theta_1 \sin(2\pi n t + \eta_1) + \theta_2 \sin(4\pi n t + \eta_2). \qquad (7)$$

Results for the other two insects are similar. For all the three droneflies, parameters specifying the wing motion are determined from the data. They include: $\bar{\phi}$ and Φ, specifying the positional angle; α_u, α_d and $\Delta\hat{t}_s$, $\Delta\hat{t}_p$, $\Delta\hat{t}_{s,t}$ and $\Delta\hat{t}_{p,t}$, specifying the angle of attack; θ_0, θ_1, θ_2, η_1 and η_2, specifying the deviation angle. The results are given in Table 2. The wing beat frequency (n), stroke plane angle (β) and body angle (χ) are also given in Table 2 [the stroke plane angle is the angle between stroke plane and the horizontal, and body angle is the angle between the long axis of the body and the horizontal (see Ellington, 1984b)].

The filmed insects are only in approximate hovering flight; i.e. some of them move at very small velocity, and the non-dimensional velocity of motion, denoted by advance ratio (J) was measured (J is the velocity of motion divided by the mean wing-tip speed $2\Phi nR$). The values of J are also included in Table 2 and are very small for the three insects.

The computed aerodynamic forces and flows

With measured wing kinematics and using the method described in Materials and methods, aerodynamic forces and moments produced by the flapping wings were computed. Since the wing motions of the three insects are similar, only the computed results for one insect, DF1, are discussed in detail here.

Let V and H be the computed vertical and horizontal forces of a wing and M the pitching moment about the center of mass. Let L and D be the lift and drag of a wing, respectively (wing lift is the force component perpendicular to the stroke plane and wing drag is the force component in the stroke plane and perpendicular to the wing span). The force and moment coefficients are defined as:

$$C_V = V / 0.5\rho U^2 S \qquad (8a)$$

$$C_H = H / 0.5\rho U^2 S \qquad (8b)$$

$$C_M = M / 0.5\rho U^2 S c \qquad (8c)$$

$$C_L = L / 0.5\rho U^2 S \qquad (8d)$$

$$C_D = D / 0.5\rho U^2 S, \qquad (8e)$$

where U is the mean velocity of the wing at r_2 ($U=\Phi n r_2$) and ρ the fluid density. Fig. 8 gives the time courses of C_V, C_H, C_M, C_L and C_D in one cycle.

The downstroke produces a little more wing lift and drag than the upstroke (see Fig. 8D,E), because the angle of attack of the downstroke is a little larger than that of the upstroke ($\alpha_d=33.8°$ and $\alpha_u=33.0°$). The vertical force is approximately the same as the wing lift (comparing Fig. 8A with D), because the stroke plane is almost horizontal (β is only 4°). From the data in Fig. 8A, the azimuthal position of the line of action of the vertical force of a downstroke or an upstroke can be calculated. The calculation shows that the line of action is near the position of the mean stroke angle, about 3° before and 5° after the position of the mean stroke angle for the downstroke and the upstroke, respectively.

As seen from the time courses of force coefficients (Fig. 8), the major part of the mean vertical force, or the mean lift, come from the mid-portions of the down- and upstrokes (the large force peaks at $\hat{t}=0.12–0.38$ and $\hat{t}=0.62–0.88$) and the contribution from wing rotation around stroke reversal is relatively small (the relatively small force peaks at $\hat{t}=0.38–0.5$ and $\hat{t}=0.88–1$). As discussed by Sun and Tang, the large C_L in the mid-portion of a down- or upstroke (during which period the wing is in pure translational motion) is due to the delayed stall mechanism, and the relatively small C_L peak near the end of the downstroke or upstroke is due to the fast pitching-up rotation of wing (Sun and Tang, 2002a). Using the data in Fig. 8, it is estimated that around 60% of the mean vertical force is contributed by the pure translational motion, or is due to the delayed stall mechanism.

The flow-field data can provide further evidence for the above statement. The contours of the non-dimensional spanwise component of vorticity at mid-span location are given in Fig. 9. The leading-edge vortex does not shed in an entire down- or upstroke, showing that the large C_L and C_D in the mid-portion of the half-stroke are due to the delayed stall mechanism.

Flight power

With the flows computed by the CFD method, the mechanical power of a wing can be easily calculated. The aerodynamic power of a wing (P_a) is:

$$P_a = \mathbf{M}_a \cdot \mathbf{\Omega}, \qquad (9)$$

where $\mathbf{M}_a$ is the aerodynamic moment around the wing root and $\mathbf{\Omega}$ the angular velocity vector of the wing. $\mathbf{M}_a$ is readily calculated using the force distribution obtained from the flow computation and $\mathbf{\Omega}$ is known from the measured data. The inertial power of the wing (P_i) is:
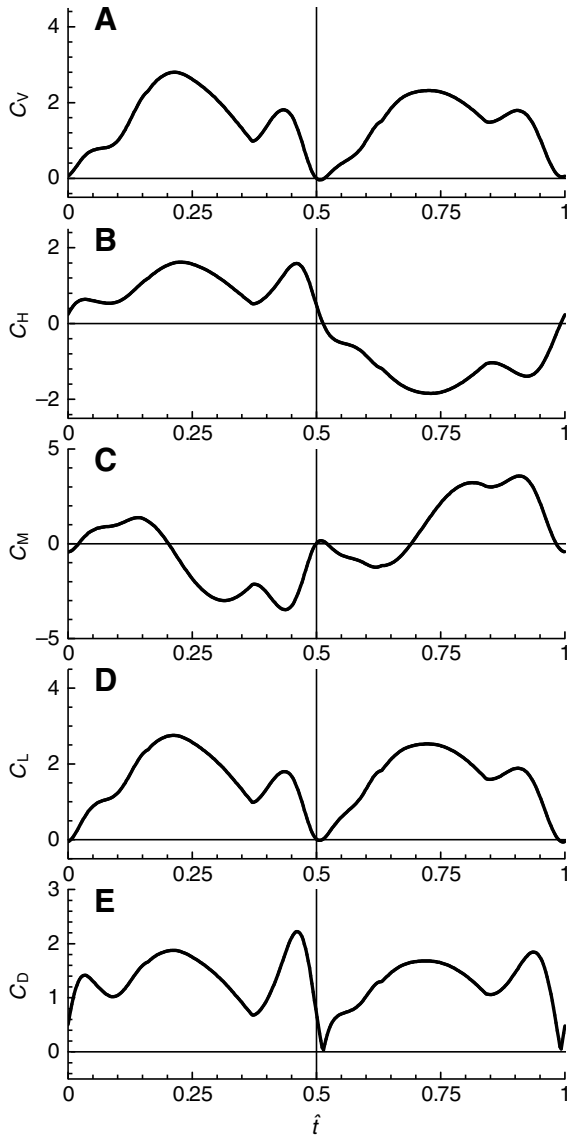
$$P_i = \mathbf{M}_i \cdot \mathbf{\Omega}, \qquad (10)$$

Fig. 8. Time courses of the computed force and moment coefficients in one cycle. $\hat{t}$, non-dimensional time; C_V and C_H, vertical and horizontal force coefficients, respectively; C_M, coefficient for pitching moment about the center of mass; C_L and C_D, wing lift and drag coefficients, respectively.

where $\mathbf{M}_i$ is the inertial moment of the wing. The way to determine $\mathbf{M}_i$ has been described previously (e.g. Sun and Tang, 2002b). The component of $\mathbf{M}_i$ due to the flip rotation of wing cannot be calculated because the moment of inertia of the wing-mass about the axis of flip rotation is not available. Since most of the wing-mass is located near the axis of flip-rotation, it is expected that this part of $\mathbf{M}_i$ is much smaller than the other parts, and is therefore neglected in the present study. The moments of inertia for the other two axes are approximately the same (denoted as I_{wg}). $I_{wg}=m_{wg}r_{2,m}^2$, where $r_{2,m}$ is the radius of gyration of I_{wg} (Ellington, 1984a). Ellington's measured data, $r_{2,m}/R=0.4$, is used here, and with data of m_{wg} in Table 1, values of I_{wg} for DF1, DF2 and DF3 are computed as 1.12×10^{-11} kg m², 1.30×10^{-11} kg m² and 1.72×10^{-11} kg m², respectively. With I_{wg} known and wing acceleration computed from Ω, $\mathbf{M}_i$ can be calculated.

The instantaneous non-dimensional power (C_p), non-dimensional aerodynamic ($C_{p,a}$) and inertial power ($C_{p,i}$) of a wing (non-dimensionalized by $0.5\rho U^2 Sc$) for DF1 are given in Fig. 10 (those for DF2 and DF3 are similar). It is interesting to note that the time course of C_p is similar to that of $C_{p,i}$; this is because the inertial power is large than the aerodynamic power. This means that elastic energy storage could be important for the droneflies.

Integrating C_p over the part of a wing-beat cycle where it is positive gives the non-dimensional positive work (C_w^+); C_w^+=20.95. Integrating C_p over the part of a wing-beat cycle where it is negative gives the non-dimensional negative work (C_w^-); C_w^-=–9.08. The mass specific power (P^*) is determined as the mean mechanical power over a wing-beat cycle divided by the mass of the insect and it can be written as:

$$P^* = 9.81\times U C_W / (\tau_c \times C_G), \qquad (11)$$

where $\tau_c=t_c U/c$ (t_c is the period of wingbeat) (Sun and Tang, 2002b). In the case of zero elastic energy storage, with the added assumption that the cost for dissipating the negative work is negligible, $C_W=C_W^+$ and P^*=60 W kg⁻¹ for DF1 (95 W kg⁻¹ and 60 W kg⁻¹ for DF2 and DF3, respectively). In the case of 100% elastic energy storage, $C_W=C_W^+-|C_W^-|$ and P^*=34.4 W kg⁻¹ for DF1 (it is 50.2 W kg⁻¹ and 38.1 W kg⁻¹ for DF2 and DF3, respectively). Thus for DF1, the largest possible effect of elastic energy storage amounts to reducing the power by about 40% (for DF2 and DF3, the value is 47% and 36%, respectively).

DISCUSSION
Wing kinematics and comparisons with available dronefly data and with fruit fly data
From the measured data of wing kinematics (Table 2), we have the following main observations. The wing beat frequency (n) of the three hovering droneflies ranges from 142 Hz to 209 Hz. The stroke amplitude (Φ) is around 110°. The downstroke angle of attack (α_d) is around 35° [the upstroke angle of attack (α_u) varies with the stroke plane angle; see below]. The stroke plane angle (β) ranges from 4° to 16.4°. When β is small, α_u is about the same as α_d (e.g. for DF1, β is 4°, α_u is 33.0°, approximately the same as α_d=33.8°); when β is relatively large (for DF2, β is about 16°), α_u is smaller than α_d by about 10°. Wing rotation time for spination is a little longer than that of pronation (e.g. for DF1, the former is 32% of the wing stroke period and the latter is 26%). Wing rotation is approximately symmetrical. The mean stroke angle ($\bar{\phi}$) also varies with β; $\bar{\phi}$ is small when β is small (for example, DF1 β=4°, $\bar{\phi}$=7.1°). The deviation angle is small, around 10°. As shown in Fig. 11A, the variation of θ gives a very shallow U-shaped wing-tip trajectory.

Comparison with available drone-fly data
Using one cine camera, Ellington measured the positional angle and deviation angle of many insects, including droneflies (Ellington, 1984b). His data show that the ϕ varies with time approximately as a simple harmonic function, and that θ is small and the wing-tip trajectory is a shallow U-shaped curve. Our data of ϕ, θ and the wing-tip trajectory agree with Ellington's [comparing Fig. 7A and Fig. 11A of the present paper with fig. 13 of Ellington (Ellington, 1984b)].

Because only one camera was used, Ellington could not measure the angle of attack. The present study has provided the time course of the angle of attack, giving data on angles of attack during downstroke and upstroke translations and rotation duration timing.

Comparison with the results of fruitflies
In a previous study, Fry et al. measured the wing kinematics of fruit flies using the same method as we use here. It is of great interest
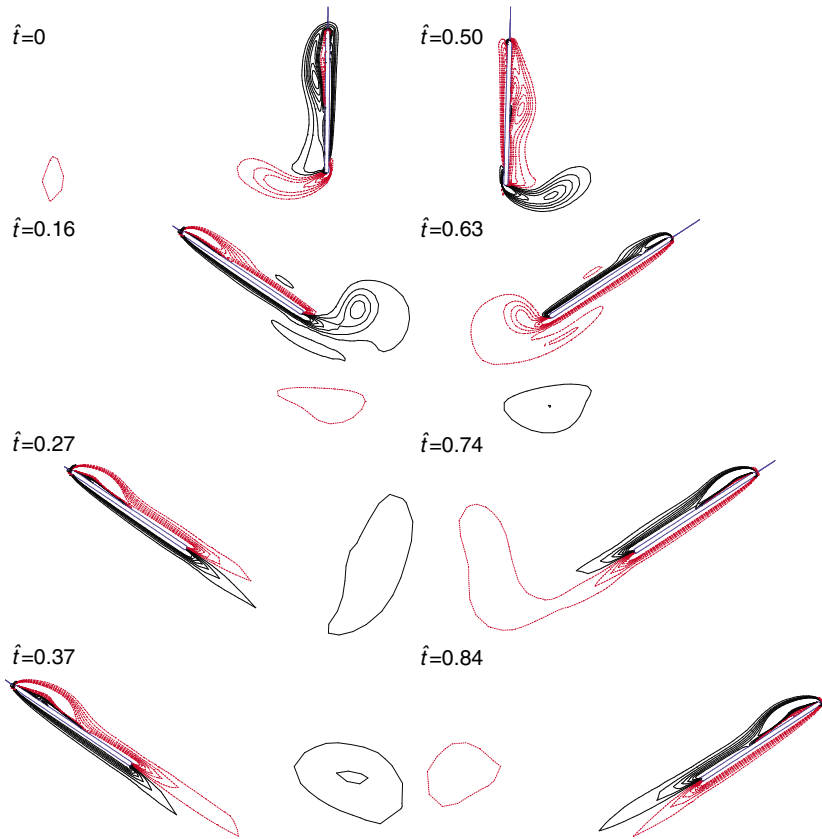
Fig. 9. Vorticity plots at r_2 at various times during one cycle. Solid and broken lines indicate positive and negative vorticity, respectively. The magnitude of the non-dimensional vorticity at the outer contour is 2 and the contour interval is 3. $\hat{t}$, non-dimensional time.

to compare the kinematics of the droneflies measured here with that of the fruit flies. For comparison, we replotted the data of the fruit flies in Fig. 12 [the data are taken from fig. 2 of Fry et al. (Fry et al., 2005); note that in Fry et al.'s paper, α is zero when the wing surface is perpendicular to the stroke plane, while in the present study α is 90° when wing is in this position, and we have converted the α values of Fry et al. to fit our definition]; data from DF1 are also given in the figure.

For both insects, φ varies with time approximately according to a simple harmonic function, except that for the fruit fly the duration of downstroke is slightly longer than that of the upstroke (comparing Fig. 12A with Fig. 12D). However, large differences in α and θ exist between the two insects.

For the fruit fly, after the supination (downstroke/upstroke) rotation and at the beginning of the following upstroke (Fig. 12B,

$\hat{t}\approx0.6$), the α value is nearly 170°, i.e. the wing chord is almost parallel to the horizontal plane, and then α decreases to about 130° near the end of the upstroke; α varies throughout the half-stroke. But for the dronefly, after the supination, α approximately keeps a constant value (around 145°) in the upstroke (Fig. 12E).

For the fruit fly, stroke deviation angle is larger, peak-to-peak amplitude is around 30°, whilst for the dronefly, this value is around 10°. As a result, the wing-tip trajectory of the fruit fly is a deep U-shaped curve and that of the dronefly a very shallow one (compare
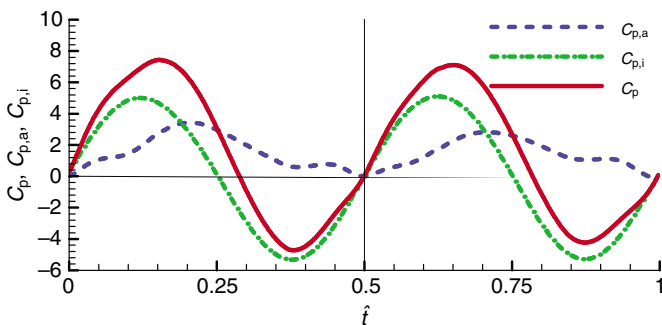

Fig. 10. Time courses of power. C_P, non-dimensional power; $C_{p,a}$ and $C_{p,i}$, non-dimensional aerodynamic and inertial power, respectively.
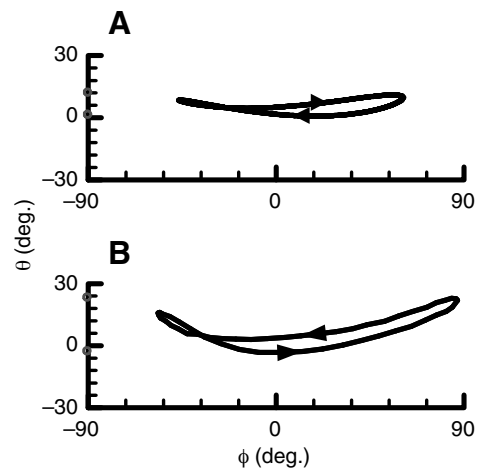

Fig. 11. (A) Wing-tip trajectory of DF1; (B) that of a fruit fly [plotted using data from Fry et al. (Fry et al., 2005)] (B). φ, the positional angle; θ, deviation angle.
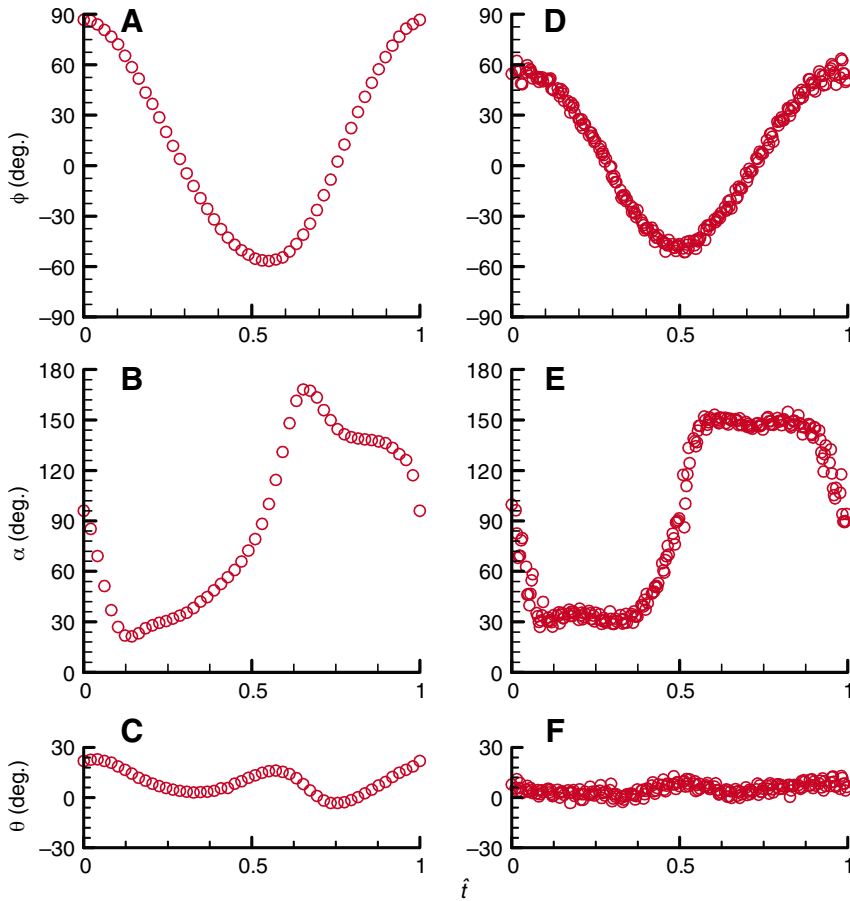
Fig. 12. Wing kinematics data. (A–C); fruit fly (data from Fry et al., 2005). (D–F); dronefly DF1. ϕ, the positional angle; α, geometrical angle of attack; θ, deviation angle; $\hat{t}$, non-dimensional time

Fig. 11A, B). Moreover, θ of the fruit fly has a fast and large decrease at the beginning of the upstroke (Fig. 12C, at $\hat{t} \approx 0.6$), shifting the minimum point of the U-shaped curve of the upstroke forward (see Fig. 11B); but for dronefly, the minimum point of the U-shaped curve is approximately at the middle (see Fig. 11A).

As discussed below, the differences in α and θ between the two insects have significant effects on how the flight is balanced.

Aerodynamic forces and flight power and comparison with the results of fruitflies

Aerodynamic forces

In their study of hovering fruit fly flight, Fry et al. 'replayed' the measured wing kinematics on a robotic model wing-pair and measured the aerodynamic forces of the wing-pair. In the present study, we used the measured wing kinematics of the droneflies in a CFD model to compute the aerodynamic forces and their corresponding moments. It is of great interest to compare the aerodynamic forces of the fruit flies and that of the droneflies.

When hovering with an approximately horizontal stroke plane, for the dronefly, the aerodynamic forces of the upstroke are a little smaller than that of the downstroke. For example, for DF1 ($\beta=4.0°$), the vertical force produced during the upstroke is approximately 11% less than that during the downstroke. By contrast, for fruit fly, the aerodynamic forces of the upstroke are larger than those of downstroke. For comparison, we have re-plotted the vertical force data of the fruit flies in Fig. 13 [using data taken from fig. 3A of Fry et al. (Fry et al., 2005)]. From the data, we estimate that the vertical force produced during the upstroke is approximately 58% larger than that during the downstroke.

For the dronefly, the vertical force that balances the insect weight is mainly produced in the mid positions of the down- and upstrokes (see Fig. 8A), during which the wing is in translational motion with constant angle of attack. Since the stroke plane is approximately horizontal and the variation of the deviation angle is small in the mid portions of the downstroke and upstroke, it can be said that the weight-supporting vertical force is mainly contributed by the lift of the wings. However, for the fruit fly, a large portion of the vertical force is produced in the early upstroke (Fig. 13). In this period of the upstroke, as discussed in Fry et al.'s paper, the wing surface is almost horizontal and the wing moves downward (Fry et al., 2005). Therefore, the vertical force produced in this period is contributed by the drag of the wings. Thus we see that when hovering with an approximately
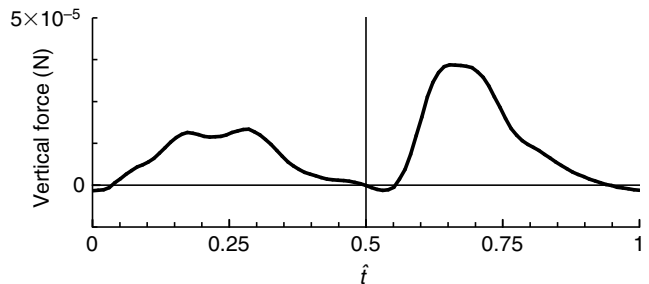

Fig. 13. Vertical force of fruit flies over the course of a stroke cycle (Fry et al., 2005).
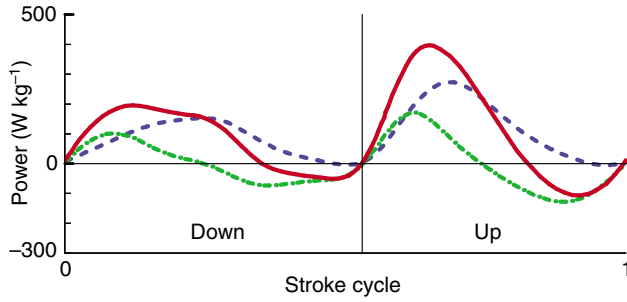
Fig. 14. Time course of power [plotted using data from Fry et al. (Fry et al., 2005)]; red solid line, total mechanic power; blue broken line, aerodynamic power component; green broken dot line, inertial power component.

horizontal stroke plane, the dronefly mainly uses the lift principle for the weight-supporting force, whilst the fruit fly uses both lift and drag principles.

Flight power

As shown above, for droneflies, the time course of mechanical power is similar to that of the inertial power (see Fig. 10), because the magnitude of inertial power is larger than the aerodynamic power. However, for the fruitflies, the inertial power is smaller than the aerodynamic power and the time course of mechanical power is similar to that of aerodynamic power [see Fig. 14 in which we have plotted the power data of the fruit flies using data from Fry et al. (Fry et al., 2005)]. As a result, droneflies could benefit from elastic energy storage much more than fruit flies: for the droneflies, the largest possible effect of elastic energy storage amounts a reduction of power by around 40%, whilst for fruit flies, the value is around 16% [calculated using data in table 1 of Fry et al. (Fry et al., 2005): $(115-97)/115=0.16$].

Let us explain why the inertial power is relatively large for the droneflies, but aerodynamic power is relatively large for the fruit flies. The inertial torque of a wing is proportional to:

$$I_{wg}\Phi n^2 = 0.5 m_{wg}\hat{r}_{2,m}^2 R^2 \Phi n^2, \qquad (12)$$

where $\hat{r}_{2,m}$ is the radius of the second moment of wing mass, normalized by R. The aerodynamic torque is proportional to:

$$\hat{r}_d \frac{\overline{C}_d}{C_G} mR = \hat{r}_d \frac{\overline{C}_d}{\overline{C}_v} mR, \qquad (13)$$

where $\overline{C}_d$ is the mean drag coefficient of wing and $\hat{r}_d$ the radius of the first moment of wing drag, normalized by R. Then, the ratio of the inertial and aerodynamic torques is proportional to:

$$\frac{m_{wg}}{m} \frac{\hat{r}_{2,m}^2}{\hat{r}_d} \frac{\overline{C}_v}{\overline{C}_d} \Phi R n^2. \qquad (14a)$$

It is assumed that $\hat{r}_d$ is approximately the same for the dronefly and fruit fly wings; measured data and computations show that droneflies and fruit flies do not have large differences in $\hat{r}_{2,m}$, Φ and $\overline{C}_v/\overline{C}_d$; $\hat{r}_{2,m}$ is around 0.4 for the droneflies (Ellington, 1984a), and around 0.48 for the fruit flies [estimated based on data of Vogel (Vogel, 1965)]; Φ is around 110° for the droneflies (Table 2), and around 140° for the fruit flies [table 1 of Fry et al. (Fry et al., 2005)]; $\overline{C}_v/\overline{C}_d$ is around 1.2 for the droneflies (calculated using the computed force data), and around 0.93 for the fruit flies [calculated using data

in table 1 of Fry et al. (Fry et al., 2005)]. Then the above ratio can be written as:

$$\frac{m_{wg}}{m} R n^2. \qquad (14b)$$

For the fruit flies, although n is a little larger than that of the droneflies [around 218 Hz (Fry et al., 2005); n for the droneflies is around 172 Hz], R and m_{wg}/m are very small [$R=2.39$ mm (Fry et al., 2005); $m_{wg}/m=0.12\%$, estimated using data of Vogel (Vogel, 1965); note that the m_{wg} is the mass of one wing]; these values are only about one fifth and one fourth of those of the droneflies, respectively], thus the inertial torque is small compared to the aerodynamic torque, resulting the small inertial power compared to the aerodynamic power. The large inertial power (compared to the aerodynamic power) for the droneflies can be explained by similar reasoning.

Flight force and moment balance and validation of the computation model

In our previous studies on flight force requirements and dynamic stability (e.g. Sun and Tang, 2002b; Sun and Wang, 2007), wing kinematic parameters for equilibrium flight, in which the forces and moments acting on the insect are balanced, must be given. Wing angles of attack (a_d and a_u) and mean stroke angle ($\overline{\phi}$) were not available and they were determined using the equilibrium flight conditions, which require the vertical force being equal to the weight and for hovering flight, the horizontal force and the pitching moment about the center of mass being zero.

Now that the angles of attack and the mean stroke angle have been measured in the present study (along with other wing kinematic parameters and the morphological parameters of wing and body), it is of interest to input all these parameters to the computation model and see whether or not an equilibrium flight is realized. This could provide a test of the computation model.

The non-dimensional weight of an insect, denoted as C_G, is defined as $C_G=mg/0.5\rho U^2(2S)$. Using data in Tables 1 and 2, values of C_G for DF1, DF2 and DF3 are computed and given in Table 3. The results of the mean vertical force, horizontal force and pitching moment coefficients ($\overline{C}_V$, $\overline{C}_H$ and $\overline{C}_M$), calculated using the computation model, are also shown in Table 3. It is seen that for all three droneflies considered, the equilibrium flight conditions are approximately met: $\overline{C}_V$ is close to C_G ($\overline{C}_V$ is different from C_G by less than 6%) and $\overline{C}_H$ and $\overline{C}_M$ are close to zero. These results show that the computation model is reasonably accurate.

Implications of the present results

Wing kinematic patterns and aerodynamic mechanisms

The present measurements on droneflies show that the wing moves at a constant angle of attack during the translational phase of a half-stroke and has a shallow U-shaped wing-tip trajectory. Based on

Table 3. Computed aerodynamic forces and moments results for hovering droneflies

ID	C_G	$\overline{C}_V$	$\overline{C}_H$	$\overline{C}_M$
DF1	1.57	1.49	−0.05	−0.06
DF2	1.51	1.59	−0.01	−0.06
DF3	1.40	1.35	0.08	−0.08

C_G, non-dimensional weight coefficient; $\overline{C}_V$, mean vertical force coefficient; $\overline{C}_H$, mean horizontal force coefficient; $\overline{C}_M$, mean pitching moment coefficient.

the wing kinematic pattern, analysis using the CFD model shows that the dronflies primarily use lift to produce weight-supporting force during the translational phase (*via* the delayed stall mechanism).

Fry et al.'s measurements on fruit flies (Fry et al., 2005) showed a very different wing kinematic pattern: the wing had a large downward plunge at the start of a half-stroke, resulting in a deep U-shaped wing-tip trajectory. Based on this wing kinematics, their experimental study using a robotic wing showed that the fruit flies rely heavily on drag mechanism during stroke reversal in producing vertical force.

These results demonstrate that insects having different wing kinematic patterns may employ different aerodynamic mechanisms for flight, and that in order to reveal the aerodynamic mechanisms an insect uses, detailed wing kinematics measurements should be conducted first. It is suggested that the studies on hovering of fruit flies (Fry et al., 2005) and dronflies (present study) are extended to other flight modes, such as forward flight and maneuver, and later on, other representative insects should be studied.

CFD method, combined with detailed kinematics measurements: a tool of great promise

An advantage of the CFD method in the study of insect flight aerodynamics and dynamics is that when the computational code is validated for an insect in a certain flight mode (for example, hovering), it can be readily used for other flight modes and for other insects. When changing from hovering to forward flight or other flight modes, only the input boundary conditions, determined by the wing motion, need to be changed, and this can be easily accomplished. When the code is used for other insects, the wing shape, hence the computational grid, and the Reynolds number in the Navier–Stokes equations need to be changed (Wu and Sun, 2004); both can be accomplished without much difficulty.

A second advantage is that the CFD method can provide any physical quantities that are needed for flow analysis. For example, aerodynamic force distribution on the wing is available, thus total aerodynamic force, moment about the center of mass of body (for flight balance study), and moment about wing root (for power calculation) can be readily obtained. Another example is that streamline patterns and vortices in the flow can be easily visualized.

The CFD model in the present study has been successfully validated for hovering dronflies. As discussed above, it can be readily used for study of other flight modes of dronflies and flight of other insects, provided that detailed wing kinematic patterns are measured. Combined with the method of 3D high-speed videography, the CFD method could be a tool of great promise in the future study of insect flight aerodynamics and dynamics.

LIST OF ABBREVIATIONS AND SYMBOLS

$\bar{c}$	mean chord length
C_D	wing drag coefficient
C_G	weight coefficient
C_H	horizontal force coefficient
$\bar{C}_H$	mean horizontal force coefficient
C_L	wing lift coefficient
C_M	pitching moment coefficient
$\bar{C}_M$	mean pitching moment coefficient
C_P	non-dimensional power
C_V	vertical force coefficient
$\bar{C}_V$	mean vertical force coefficient
C_w	non-dimensional work per cycle
C_w^+	non-dimensional positive work per cycle
C_w^-	non-dimensional negative work per cycle
CFD	computational fluid dynamics
D	drag of a wing
$\boldsymbol{g}$	the gravitational acceleration
h_1	distance from wing-root axis to long-axis of body
H	horizontal force
I_{wg}	moment of inertia of the wing about wing root
I_y	moment of inertia of the body about center of mass
J	advance ratio
l_b	body length
l_r	distance between two wing roots
l_1	distance from wing-root axis to body center of mass
L	lift of a wing
LED	light emitting diode
m	mass of an insect
m_{wg}	mass of one wing
$\mathbf{M}_a$	aerodynamic moment of wing around wing root
$\mathbf{M}_i$	inertial moment of wing around wing root
M_y	pitching moment about center of mass
n	stroke frequency
P_a	aerodynamic power
P_i	inertial power
P^*	body-mass-specific power
r_2	radius of the second moment of wing area
$r_{2,m}$	radius of the second moment of wing mass
r_d	radius of the first moment of wing drag
R	wing length
S	area of one wing
t	time
t_c	period of wing beat
$\hat{t}$	non-dimensional time ($\hat{t}$=0 and 1 at the start and end of a cycle, respectively)
U	reference velocity (mean flapping velocity at r_2)
V	vertical force of a wing
α	angle of attack
α_d	constant value of α at the mid-position of the downstroke
α_u	constant value of α at the mid-position of the upstroke
β	stroke plane angle
$\Delta\hat{t}_p$	non-dimensional time duration for pronation
$\Delta\hat{t}_{p,t}$	non-dimensional advance time for pronation
$\Delta\hat{t}_s$	non-dimensional time duration for supination
$\Delta\hat{t}_{s,t}$	non-dimensional advance time for spination
η_1	phase angle of the first harmonic of Fourier series of deviation angle
η_2	phase angle of the second harmonic of Fourier series of deviation angle
θ	deviation angle
θ_0	constant value of Fourier series of deviation angle
θ_1	amplitude of the first harmonic of Fourier series of deviation angle
θ_2	amplitude of the second harmonic term of deviation angle
ρ	density of fluid
υ	kinematic viscosity of fluid
ϕ	positional angle
$\bar{\phi}$	mean positional angle
Φ	stroke amplitude
χ	body angle
χ_0	free body angle
Ω	wing rotation velocity vector

REFERENCES

Dickinson, M. H., Lehmann, F. O. and Sane, S. P. (1999). Wing rotation and the aerodynamic basis of insect flight. *Nature* **284**,1954-1960.

Dudley, R. and Ellington, C. P. (1990). Mechanics of forward flight in bumblebees. I. Kinematics and morphology. *J. Exp. Biol.* **148**, 19-52.

Ellington, C. P. (1984a). The aerodynamics of hovering insect flight. II. Morphological parameters. *Philos. Trans. R. Soc. Lond. B Biol. Sci.* **305**, 1-15.

Ellington, C. P. (1984b). The aerodynamics of hovering insect flight. III. Kinematics. *Philos. Trans. R. Soc. Lond. B Biol. Sci.* **305**, 17-40.

Fry, S. N., Sayaman, R. and Dickinson, M. H. (2005). The aerodynamics of hovering flight in *Drosophila*. *J. Exp. Biol.* **208**, 2303-2318.

Lehmann, F. O., Sane, S. P. and Dickinson, M. H. (2005). The aerodynamic effects of wing–wing interaction in flapping insect wings. *J. Exp. Biol.* **208**, 3075-3092.

Sun, M. and Tang, J. (2002a). Unsteady aerodynamic force generation by a model fruit fly wing in flapping motion. *J. Exp. Biol.* **205**, 55-70.

Sun, M. and Tang, J. (2002b). Lift and power requirements of hovering flight in *Drosophila virilis. J. Exp. Biol.* **205**, 2413-2427.

Sun, M. and Wang, J. K. (2007). Flight stabilization control of a hovering model insect. *J. Exp. Biol.* **210**, 2714-2722.

Sun, M. and Yu, X. (2006). Aerodynamic force generation in hovering flight in a tiny insect. *AIAA J.* **44**, 1532-1540.

Usherwood, J. R. and Ellington, C. P. (2002a). The aerodynamics of revolving wings. I. Model hawkmoth wings. *J. Exp. Biol.* **205**, 1547-1564.

Usherwood, J. R. and Ellington, C. P. (2002b). The aerodynamics of revolving wings. II. Propeller force coefficients from mayfly to quail. *J. Exp. Biol.* **205**, 1565-1574.

Vogel, S. (1965). Flight in *Drosophila* I. Flight performance of tethered flies. *J. Exp. Biol.* **44**, 567-578.

Willmott, A. P. and Ellington, C. P. (1997). The mechanics of flight in the hawkmoth *Manduca sexta.* I. Kinematics of hovering and forward flight. *J. Exp. Biol.* **384**, 2705-2722.

Wu, J. H. and Sun, M. (2004). Unsteady aerodynamic forces of a flapping wing. *J. Exp. Biol.* **207**, 1137-1150.